# Elastic waves in helical waveguides

Fabien Treyssède

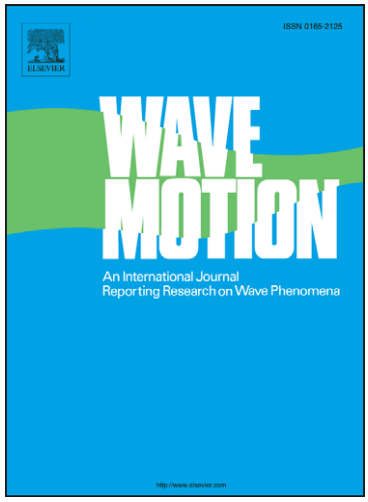


Elastic waves in helical waveguides

Fabien Treyssède

PII: S0165-2125(07)00098-4
DOI: 10.1016/j.wavemoti.2007.09.004
Reference: WAMOT 1399

To appear in: *Wave Motion*

Received Date: 13 July 2007
Revised Date: 6 September 2007
Accepted Date: 20 September 2007

Please cite this article as: F. Treyssède, Elastic waves in helical waveguides, *Wave Motion* (2007), doi: 10.1016/j.wavemoti.2007.09.004

# Elastic waves in helical waveguides

Fabien TREYSSÈDE

Nantes Atlantique Université, LCPC, DMI

BP 4129, 44341 Bouguenais, FRANCE

E-mail : fabien.treyssede@lcpc.fr

Received:

Abstract:

The goal of this paper is to theoretically investigate the propagation of elastic waves in helical waveguides. In the context of non-destructive evaluation for structural health monitoring, this study is motivated by the need for inspecting helical structures such as cables or springs. A numerical method is chosen based on a semi-analytical finite element technique. The proposed method relies on a non-orthogonal curvilinear coordinate system that is translationally invariant along the helix centreline, so that a Fourier transform is explicitly performed and the problem is reduced to two dimensions. Some useful expressions are also derived for the averaged energy and flux in order to directly compute the energy velocity. The convergence and accuracy of the proposed method are then assessed by comparing finite element results with reference solutions. A dispersion analysis inside a 7.5° helical wire, typically encountered in civil engineering cables, is realised including attenuation due to material damping. Some dispersion curves are finally presented for a wide range of lay angles and for several centreline radii. Significant differences with the infinite cylinder are observed.

Keywords: propagation, elastic, helical, waveguide, semi-analytical, finite element

## 1. INTRODUCTION

As an interesting non-destructive test technology for structural health monitoring, elastic guided waves have received a great deal of attention. In cylindrical waveguides, elastic wave propagation has been widely investigated since the early works of Pochhammer in 1876 and Chree in 1889. For instance, we can cite the paper of Zemanek [1], who was one of the first authors to present a complete analytical and experimental investigation. However, similar attention has not been given to helical waveguides, though their study might be important for inspecting helical structures such as cables or springs.

In civil engineering, a typical application is given by steel multi-wire cables, which are widely employed as load-carrying members. The basic element of these cables is usually a simple straight strand made of a straight core and one layer of helical wires. Some recent experimental studies of multi-wire strands have been realized pointing out the fact that the Pochhammer-Chree dispersion curves cannot accurately predict propagation inside multi-wire strands [2–6]. In fact, the theoretical understanding of guided ultrasonic waves in multi-wire strands is complicated by the helical geometry of peripheral wires, the inter-wire coupling and contact effects, the presence of applied loads and concrete embedment (if any) [3–8]. As a first step toward an increasing complexity, only the first above complicating effect is addressed in this paper by numerically investigating elastic guided waves inside a single helical wire.

Since this work aims at improving the understanding of such guided waves, a computational approach rather than a purely mathematical approach has been chosen. In order to deal with complex geometry, some of the most popular and efficient numerical techniques are based on finite element (FE) methods.

The so-called semi-analytical finite element (SAFE) method is a first approach that has been used to study uniform straight waveguides of arbitrary cross-section – see for instance Refs. [9–15]. Using an interesting procedure based on the use of an axisymmetric harmonic FE code, toroidal waveguides have also been considered by Demma et al. [16] but only real wavenumbers and a limited number of wavenumbers can be handled with this procedure (in particular, modes with imaginary or complex wavenumbers cannot be dealt with). Onipede et al. [17,18] developped a SAFE method in order to study uniformly pretwisted waveguides along a straight axis. Assuming an exponential dependence of the form $e^{i(kz-\omega t)}$ (where $k$ is the wavenumber, $z$ the axis waveguide, and $\omega$ is the frequency), SAFE methods are interesting from a computational point of view because only the cross-section has to meshed, hence drastically reducing the number of degrees of freedom (dofs).

A second approach is based on the theory of wave propagation in periodic structures, which is somewhat more general because non-uniform waveguides can be analyzed. Based on Floquet's principle, this theory allows studying the single repetitive

substructure alone, thanks to the application of a set of periodic boundary conditions involving a propagation constant corresponding to the eigenvalue. A review on the topic can be found in Ref. [19]. Based on a general theory presented by Mead [20], some periodic FE approaches and procedures have then been developed – see for instance Refs. [21−24]. Such methods can be implemented as a post-process step of a standard FE code providing stiffness, mass and damping matrices. Similarly to SAFE methods, periodic FE approaches only need the mesh of one repetitive cell, which reduces the computational cost.

For modelling a single helical wire, which is a uniform waveguide, both SAFE and periodic FE approaches can be applied. The author [25] has recently proposed a numerical procedure based on a periodic FE approach combined with a specific helical mapping in order to arbitrarily reduce the periodic cell length. He presented results for an undamped helical wire having a 7.5° lay angle, typically encountered in seven-wire strands. In this paper, a SAFE method extended to helical waveguides is proposed. In Sec. 2, a weak variational formulation is written in terms of a non-orthogonal curvilinear coordinate system that is translationally invariant along the helix centreline, so that a Fourier transform is explicitly performed. As opposed to a periodic FE approach, this approach explicitly takes into account the property of translational invariance of helical waveguides. More mathematical insight is somewhat gained and the problem to be solved is reduced to two dimensions (computational costs are thus reduced). Note that the coordinate system used can be considered as an extension of the

works of Onipede et al. [17,18] developed for pretwisted waveguides. In Sec. 3, after some considerations about convergence and accuracy of the SAFE method, a dispersion analysis inside a 7.5° helical wire is realised including attenuation due to material damping. Some dispersion curves are finally presented for a wide range of lay angles and for several centreline radii.

## 2. FE FORMULATION FOR HELICAL WAVEGUIDES

In this section, a SAFE method is presented to solve the propagation modes of a helical waveguide having any arbitrary cross-section (not necessarily circular). The reader can be referred to [26] (for instance) for a fundamental introduction about the use of general curvilinear coordinate systems.

### 2.1. Curvilinear coordinate system for translational invariance

The helix centreline curve can be described by the following position vector:

$$\mathbf{R}(s) = R\cos\left(\frac{2\pi}{l}s\right)\mathbf{e}_X + R\sin\left(\frac{2\pi}{l}s\right)\mathbf{e}_Y + \frac{L}{l}s\mathbf{e}_Z \tag{1}$$

where $l = \left(L^2 + 4\pi^2 R^2\right)^{1/2}$. $\left(\mathbf{e}_X, \mathbf{e}_Y, \mathbf{e}_Z\right)$ denotes the cartesian orthonormal basis. $R$ and $L$ are respectively the radius of the centreline in the $(X,Y)$ cartesian plane and the helix step along the $Z$ cartesian axis (see Fig. 1a). A complete period is described by the parameter $s$ varying from 0 to $l$. It should be noted that the parameter $s$ has been chosen so that it corresponds to the arc length ($l$ is thus the curvilinear length of one helix step). The unit tangent vector to the centreline is then directly given by $\mathbf{T} = d\mathbf{R}/ds$. The unit

normal can be defined from the Serret-Frenet formulae $d\mathbf{T}/ds = \kappa\mathbf{N}$, and the unit binormal vector is $\mathbf{B} = \mathbf{T} \wedge \mathbf{N}$. The following Serret-Frenet formulae also holds: $d\mathbf{N}/ds = \tau\mathbf{B} - \kappa\mathbf{T}$, $d\mathbf{B}/ds = -\tau\mathbf{N}$. For the curve defined by (1), both the curvature $\kappa$ and the tortuosity $\tau$ are constant: $\kappa = 4\pi^2 R/l^2$ and $\tau = 2\pi L/l^2$.

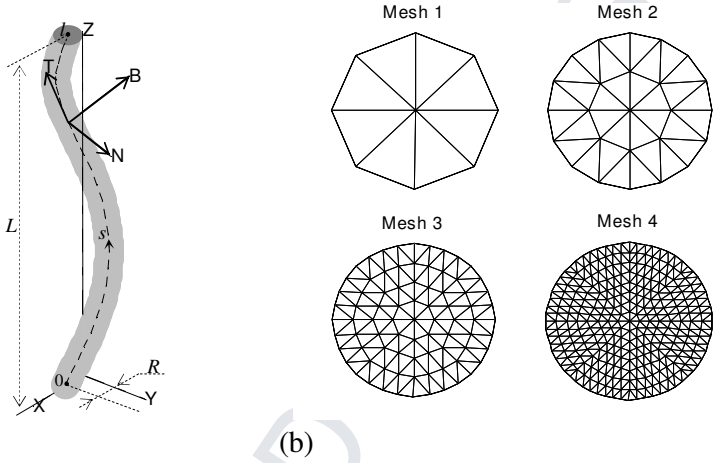


FIG.1: (a) One step of a helical waveguide of circular cross-section with its centreline (dashed line) and its local basis $(\mathbf{N}, \mathbf{B}, \mathbf{T})$. (b) Cross-section meshes 1 to 4 with successive refinements.

Now, a new coordinate system ($x$,$y$,$s$) is constructed from the orthonormal basis $(\mathbf{N}, \mathbf{B}, \mathbf{T})$, for which any Cartesian vector $\mathbf{X}$ can be expressed as:

$$\mathbf{X}(x, y, s) = \mathbf{R}(s) + x\mathbf{N}(s) + y\mathbf{B}(s) \tag{2}$$

Using the above Serret-Frenet formulae, it can be shown that this kind of mapping yields the following non-orthogonal covariant basis $\left(\partial\mathbf{X}/\partial x, \partial\mathbf{X}/\partial y, \partial\mathbf{X}/\partial s\right)$, denoted by $\left(\mathbf{g}_1, \mathbf{g}_2, \mathbf{g}_3\right)$:

$$\mathbf{g}_1 = \mathbf{N}(s) \quad , \quad \mathbf{g}_2 = \mathbf{B}(s) \quad , \quad \mathbf{g}_3 = (1-\kappa x)\mathbf{T}(s) + \tau x \mathbf{B}(s) - \tau y \mathbf{N}(s) \tag{3}$$

The covariant metric tensor of such a mapping, defined by $g_{mn} = \mathbf{g}_m \cdot \mathbf{g}_n$, is then given by:

$$\mathbf{g} = \begin{bmatrix} 1 & 0 & -\tau y \\ 0 & 1 & \tau x \\ -\tau y & \tau x & \tau^2\left(x^2+y^2\right) + (1-\kappa x)^2 \end{bmatrix} \tag{4}$$

**g** does not depend on the third curvilinear coordinate *s* because $\kappa$ and $\tau$ are constant for a helix. Provided that the cross-section of the waveguide does not vary along *s* nor the material properties, this means that this curvilinear coordinate system yields a translational invariance along *s*.

The contravariant basis $\left(\mathbf{g}^1, \mathbf{g}^2, \mathbf{g}^3\right)$, defined by $\mathbf{g}^i \cdot \mathbf{g}_j = \delta^i_j$ is given by:

$$\mathbf{g}^1 = \frac{\tau y}{1-\kappa x}\mathbf{T}(s) + \mathbf{N}(s) \quad , \quad \mathbf{g}^2 = -\frac{\tau x}{1-\kappa x}\mathbf{T}(s) + \mathbf{B}(s) \quad , \quad \mathbf{g}^3 = \frac{1}{1-\kappa x}\mathbf{T}(s) \tag{5}$$

yielding the following contravariant metric tensor, defined by $g^{mn} = \mathbf{g}^m \cdot \mathbf{g}^n$:

$$\mathbf{G} = \mathbf{g}^{-1} = \frac{1}{g}\begin{bmatrix} g + (\tau y)^2 & -\tau^2 xy & \tau y \\ -\tau^2 xy & g + (\tau x)^2 & -\tau x \\ \tau y & -\tau x & 1 \end{bmatrix} \tag{6}$$

where $g=(1-\kappa x)^2$ is the determinant of **g**. The Christoffel symbol of the second kind $\Gamma_{ij}^k$, defined by $\Gamma_{ij}^k=\mathbf{g}_{i,j}\cdot\mathbf{g}^k$, can be calculated from the Serret-Frenet formulae which gives:

$$\begin{aligned}
&\Gamma_{11}^k=\Gamma_{12}^k=\Gamma_{21}^k=\Gamma_{22}^k=0\ ,\ \Gamma_{23}^2=\Gamma_{32}^2=\Gamma_{23}^3=\Gamma_{32}^3=0,\\
&\Gamma_{33}^1=\frac{\kappa(\tau y)^2}{1-\kappa x}+\kappa(1-\kappa x)-\tau^2 x\ ,\ \Gamma_{33}^2=-\frac{\kappa\tau^2 xy}{1-\kappa x}-\tau^2 y\ ,\ \Gamma_{33}^3=\frac{\kappa\tau y}{1-\kappa x},\\
&\Gamma_{13}^1=\Gamma_{31}^1=-\frac{\kappa\tau y}{1-\kappa x}\ ,\ \Gamma_{23}^1=\Gamma_{32}^1=-\tau\ ,\ \Gamma_{13}^2=\Gamma_{31}^2=\frac{\kappa\tau x}{1-\kappa x}+\tau\ ,\ \Gamma_{13}^3=\Gamma_{31}^3=-\frac{\kappa}{1-\kappa x}
\end{aligned}\tag{7}$$

It should be noted that *x* and *y* must remain small enough on the cross-section in order to the so defined coordinates $(x,y,s)$ to be single valued (in particular, *g* must remain non-zero, i.e. $\kappa x<1$). This restriction will be implied in the remaining.

### 2.2. Variational formulation

Assuming a linearly elastic material, small strains and displacements and a time harmonic $e^{-i\omega t}$ dependence, the 3D variational formulation governing dynamics is given by:

$$\int_\Omega \delta\boldsymbol{\varepsilon}:\boldsymbol{\sigma}dV-\omega^2\int_\Omega \rho\delta\mathbf{u}\cdot\mathbf{u}dV=0 \tag{8}$$

for any kinematically admissible trial field $\delta\mathbf{u}$. $\mathbf{u}$ and $\boldsymbol{\sigma}$ respectively denote the displacement vector field and the Cauchy stress tensor. $\rho$ is the material density and $\Omega$ represents the structural volume. Of course, there is no external body force for the purpose of studying propagation modes. Besides, the waveguide is assumed to be subjected to some traction-free or zero-displacement boundary conditions on its external

boundary (making any surface integrals vanish). The stress-strain and strain-displacement relations are respectively given by $\boldsymbol{\sigma} = \mathbf{C} : \boldsymbol{\varepsilon}$ and $\boldsymbol{\varepsilon} = 1/2\left(\nabla \mathbf{u} + \nabla \mathbf{u}^T\right)$.

The formulation (8) must first be written in a general non-orthogonal curvilinear coordinate system. Using product and differentiation rules of such a system (see for instance Ref. [27] or Chapter 2 of Ref. [28]), it can be shown that the stress-strain and strain-displacement relations becomes:

$$\sigma^{ij} = C^{ijkl}\varepsilon_{kl} \quad , \quad \varepsilon_{ij} = 1/2\left(u_{i,j} + u_{j,i}\right) - \Gamma^k_{ij} u_k \tag{9}$$

where subscripts (resp. superscripts) denote covariant (resp. contravariant) components with respect to the contravariant basis $\left(\mathbf{g}^1, \mathbf{g}^2, \mathbf{g}^3\right)$ (resp. covariant basis $\left(\mathbf{g}_1, \mathbf{g}_2, \mathbf{g}_3\right)$). The notation $\left(\cdot\right)_{,i}$ ($i$=1,2,3) is used for derivatives with respect to $x$, $y$ and $s$ respectively. Besides, the following rules also hold for the dot and double dot products: $\delta\boldsymbol{\varepsilon} : \boldsymbol{\sigma} = \delta\varepsilon_{ij}\sigma^{ij}$ , $\delta\mathbf{u} \cdot \mathbf{u} = \delta u_i g^{ij} u_j$. Note that the covariant displacement components are non-physical (they do not have the dimensions of length, physical components being given by $u_{(i)} = \sqrt{g^{ii}}\, u_i$ without summation over $i$). In this paper, physical components with respect to the orthonormal $\left(\mathbf{N}, \mathbf{B}, \mathbf{T}\right)$ basis are preferred, and it can be shown that the following relationship holds:

$$u_i = Q_{i\alpha} u_\alpha \qquad \text{, with: } \mathbf{Q} = \begin{bmatrix} 1 & 0 & 0 \\ 0 & 1 & 0 \\ -\tau y & \tau x & 1 - \kappa x \end{bmatrix} \tag{10}$$

where the greek subscript $\alpha = n, b, t$ denotes components with respect to $\left(\mathbf{N}, \mathbf{B}, \mathbf{T}\right)$.

Using the symmetry properties of stress and strain tensors, the variational formulation (8) might be rewritten as follows:

$$\int_\Omega \delta\boldsymbol{\varepsilon}^T \boldsymbol{\sigma} \sqrt{g}\, dxdyds - \omega^2 \int_\Omega \rho \delta \mathbf{u}^T \mathbf{Q}^T \mathbf{G} \mathbf{Q} \mathbf{u} \sqrt{g}\, dxdyds = 0 \tag{11}$$

with the notations $\delta\mathbf{u}=\left[\delta u_n \quad \delta u_b \quad \delta u_t\right]^T$, $\delta\boldsymbol{\varepsilon}=\left[\delta\varepsilon_{11} \quad \delta\varepsilon_{22} \quad \delta\varepsilon_{33} \quad 2\delta\varepsilon_{12} \quad 2\delta\varepsilon_{13} \quad 2\delta\varepsilon_{23}\right]^T$, and $\boldsymbol{\sigma}=\left[\sigma^{11} \quad \sigma^{22} \quad \sigma^{33} \quad \sigma^{12} \quad \sigma^{13} \quad \sigma^{23}\right]^T$, and where it can be shown that $\mathbf{Q}^T\mathbf{G}\mathbf{Q}=\mathbf{I}$. The stress-strain relationship is now written $\boldsymbol{\sigma}=\mathbf{C}\boldsymbol{\varepsilon}$, with:

$$\mathbf{C}=\begin{bmatrix} C^{1111} & C^{1122} & C^{1133} & C^{1112} & C^{1113} & C^{1123} \\ & C^{2222} & C^{2233} & C^{2212} & C^{2213} & C^{2223} \\ & & C^{3333} & C^{3312} & C^{3313} & C^{3323} \\ & & & C^{1212} & C^{1213} & C^{1223} \\ & sym & & & C^{1313} & C^{1323} \\ & & & & & C^{2323} \end{bmatrix} \tag{12}$$

It must be outlined that in Eq. (12), the components of $\mathbf{C}$ must be expressed with respect to the covariant basis. For an isotropic material, they are:

$$C^{ijkl}=\frac{\nu E}{(1+\nu)(1-2\nu)} g^{ij} g^{kl} + \frac{E}{2(1+\nu)}\left(g^{ik} g^{jl} + g^{il} g^{jk}\right) \tag{13}$$

$E$ is the Young modulus and $\nu$ denotes the Poisson coefficient.

For the helical coordinate system previously defined and using Eqs. (7) and (10) into (9), it can be shown that the following strain-displacement relation is obtained:

$$\boldsymbol{\varepsilon}=\left(\mathbf{L}_{xy}+\partial/\partial s\, \mathbf{L}_s\right)\mathbf{u} \tag{14}$$

with the operators $\mathbf{L}_{xy}$ and $\mathbf{L}_s$:

$$\mathbf{L}_{xy}=\begin{bmatrix} \partial/\partial x & 0 & 0 \\ 0 & \partial/\partial y & 0 \\ \tau^2 x-\kappa(1-\kappa x) & \tau^2 y & -\kappa\tau y \\ \partial/\partial y & \partial/\partial x & 0 \\ -\tau y\,\partial/\partial x & -\tau+\tau x\partial/\partial x & \kappa+(1-\kappa x)\partial/\partial x \\ \tau-\tau y\,\partial/\partial y & \tau x\partial/\partial y & (1-\kappa x)\partial/\partial y \end{bmatrix},\ \mathbf{L}_s=\begin{bmatrix} 0 & 0 & 0 \\ 0 & 0 & 0 \\ -\tau y & \tau x & 1-\kappa x \\ 0 & 0 & 0 \\ 1 & 0 & 0 \\ 0 & 1 & 0 \end{bmatrix} \quad (15)$$

### 2.3. Semi-analytical FE method

The helical transformation previously defined allows the investigation of the propagation modes because $s$ does not appear explicitly in the equilibrium equations written in the curvilinear system, except for derivatives with respect to $s$. A Fourier transform in the $s$ direction can thus be performed so that we can still speak of propagation modes. Hence, an exponential $e^{iks}$ might be separated from all field component, and $\partial/\partial s$ replaced by $ik$, where $k$ denotes the axial wavenumber (along the helix centreline). It has to be pointed out that similar kinds of helical mapping had already been considered in electromagnetics to study helical waveguides, analytically [29] or numerically [30].

The displacement vector and the trial field are now rewritten as:

$$\mathbf{u}=\mathbf{u}(x,y)e^{i(ks-\omega t)}\ ,\ \delta\mathbf{u}=\delta\mathbf{u}(x,y)e^{-i(ks-\omega t)} \quad (16)$$

Using Eqs. (16) and (14) into (11) yields the following semi-analytical variational formulation, now reduced on an integration on the waveguide cross-section:

$$\begin{aligned}&\int_S \delta\mathbf{u}^T\mathbf{L}_{xy}^T\mathbf{C}\mathbf{L}_{xy}\mathbf{u}\sqrt{g}\,dxdy + ik\int_S \delta\mathbf{u}^T\left(\mathbf{L}_{xy}^T\mathbf{C}\mathbf{L}_s - \mathbf{L}_s^T\mathbf{C}\mathbf{L}_{xy}\right)\mathbf{u}\sqrt{g}\,dxdy\\&+k^2\int_S \delta\mathbf{u}^T\mathbf{L}_s^T\mathbf{C}\mathbf{L}_s\mathbf{u}\sqrt{g}\,dxdy - \omega^2\int_S \rho\delta\mathbf{u}^T\mathbf{G}\mathbf{u}\sqrt{g}\,dxdy = 0\end{aligned} \tag{17}$$

This variational problem can be solved using standard 2D Lagrange finite elements, which have three degrees of freedom per node associated with $u_n, u_b, u_t$. On a given element, the covariant components of the displacement are then approximated as follows:

$$\mathbf{u} = \mathbf{N}^e\mathbf{U}^e \tag{18}$$

$\mathbf{N}^e$ is a matrix containing nodal interpolating functions and $\mathbf{U}^e$ is a column vector containing the nodal displacements of the element. For instance, the interpolation for linear three-node triangles is given by $u_\alpha = (1-\xi-\eta)u_\alpha^1 + \xi u_\alpha^2 + \eta u_\alpha^3$ ($\alpha$=n,b,t), where the superscripts denote the local node number and $\xi$ and $\eta$ are the reference coordinates of the element varying from 0 to +1.

The FE discretisation of the formulation (17) finally yields the following eigenvalue problem:

$$\left\{\mathbf{K}_1 - \omega^2\mathbf{M} + ik\left(\mathbf{K}_2 - \mathbf{K}_2^T\right) + k^2\mathbf{K}_3\right\}\mathbf{U} = 0 \tag{19}$$

with the elementary matrices given by:

$$\begin{aligned}&\mathbf{K}_1^e = \int_{S^e}\mathbf{N}^{eT}\mathbf{L}_{xy}^T\mathbf{C}\mathbf{L}_{xy}\mathbf{N}^e\sqrt{g}\,dxdy \;,\; \mathbf{K}_2^e = \int_{S^e}\mathbf{N}^{eT}\mathbf{L}_{xy}^T\mathbf{C}\mathbf{L}_s\mathbf{N}^e\sqrt{g}\,dxdy,\\&\mathbf{K}_3^e = \int_{S^e}\mathbf{N}^{eT}\mathbf{L}_s^T\mathbf{C}\mathbf{L}_s\mathbf{N}^e\sqrt{g}\,dxdy \;,\; \mathbf{M}^e = \int_{S^e}\rho\mathbf{N}^{eT}\mathbf{G}\mathbf{N}^e\sqrt{g}\,dxdy\end{aligned} \tag{20}$$

Because of the symmetry of $\mathbf{K}_1$, $\mathbf{K}_3$ and $\mathbf{M}$ and using the property $\det \mathbf{A}^T = \det \mathbf{A}$ ($\mathbf{A}$ is any matrix), it can easily be checked that if $k$ is an eigenvalue of (19), then $-k$ is also an eigenvalue. Hence, the eigenproblem has two sets of eigensolutions $(k_j, \mathbf{U}_j^+)$ and $(-k_j, \mathbf{U}_j^-)$ $(j = 1, \ldots, n)$, representing $n$ positive-going and $n$ negative-going wave types ($n$ being the number of dofs). In the absence of damping, eigenvalues for which $k_j$ is purely real (resp. imaginary) represent propagating (resp. evanescent) waves and those for which $k_j$ is fully complex are inhomogeneous waves (decaying but oscillatory).

At fixed real $k$, the eigenproblem (19) is linear for finding $\omega^2$. However this simpler approach is useful only if interest is restricted to propagating modes in undamped systems. Given $\omega$ and finding $k$, the eigenproblem is then quadratic and must be recast into a generalized linear eigensystem in order to be solved with standard numerical solvers. This can be done as follows:

$$\left( \begin{bmatrix} \mathbf{0} & \mathbf{K}_1 - \omega^2 \mathbf{M} \\ \mathbf{K}_1 - \omega^2 \mathbf{M} & i\left(\mathbf{K}_2 - \mathbf{K}_2^T\right) \end{bmatrix} - k \begin{bmatrix} \mathbf{K}_1 - \omega^2 \mathbf{M} & \mathbf{0} \\ \mathbf{0} & -\mathbf{K}_3 \end{bmatrix} \right) \begin{bmatrix} \mathbf{U} \\ k\mathbf{U} \end{bmatrix} = \begin{bmatrix} \mathbf{0} \\ \mathbf{0} \end{bmatrix} \tag{21}$$

In the absence of material damping, this eigensystem is hermitian. The purely real and imaginary solutions appear in pairs of opposite signs, while the fully complex solutions appear in quadruples of complex conjugates and opposite signs (if $k$ is an eigenvalue, then $-k$, $k^*$ and $-k^*$ are also eigenvalues). With material damping, this is not the case any more and every roots simply appear in pairs of opposite signs.

### 2.4. Energy velocity

The cross-section and time averaged energy velocity in waveguides is defined as follows:

$$v_e = \int_S \overline{\mathbf{P}} \cdot \mathbf{n} dS \Big/ \int_S \left( \overline{E}_k + \overline{E}_p \right) dS \tag{22}$$

where bars denote time averaging. **n** is the unit vector along the propagation direction (i.e. normal to the cross-section). $P^i$ is the *i*th contravariant component of Poynting vector, $E_k$ and $E_p$ are the kinetic and potential energies, given by:

$$P^i = -\sigma^{ij} \dot{u}_j \quad , \quad E_k = \frac{1}{2} \rho \dot{u}_i g^{ij} \dot{u}_j \quad , \quad E_p = \frac{1}{2} \varepsilon_{ij} \sigma^{ij} \tag{23}$$

It should be noted that the energy velocity is a wave property that remains appropriate for damped media, as opposed to the group velocity definition $v_g = \partial \omega / \partial k$ that is generally not valid in damped waveguides [31].

Having solved the eigensystems (19) or (21), the energy velocity of a given mode $(k, \mathbf{U})$ can be directly post-processed from the matrices previously defined in Sec. 2.3. First, it can be easily deduced that:

$$\int_S \overline{E}_k dS = \frac{\omega^2}{4} \mathrm{Re}\left( \mathbf{U}^{T*} \mathbf{M} \mathbf{U} \right) \quad , \quad \int_S \overline{E}_p dS = \frac{1}{4} \mathrm{Re}\left\{ \mathbf{U}^{T*} \left( \mathbf{K}_1 + ik \left( \mathbf{K}_2 - \mathbf{K}_2^T \right) + k^2 \mathbf{K}_3 \right) \mathbf{U} \right\} \tag{24}$$

The computation of the cross-section and time averaged Poynting vector requires further developments but can also be simply expressed. Noticing that $\mathbf{n} = \mathbf{T} = (1-\kappa x)\mathbf{g}^3$ and $dS = dxdy$, we have:

$$\bar{\mathbf{P}} \cdot \mathbf{n} dS = \frac{\omega}{2} \mathrm{Im}\left\{ u_i^* \sigma^{i3} (1-\kappa x)\, dxdy \right\} \tag{25}$$

Then, it can be checked that $u_i^* \sigma^{i3} = \mathbf{u}^* \mathbf{L}_s{}^T \boldsymbol{\sigma} = \mathbf{u}^* \mathbf{L}_s{}^T \mathbf{C}\left(\mathbf{L}_{xy} + ik\mathbf{L}_s\right)\mathbf{u}$, so that the following interesting expression holds for the averaged Poynting vector:

$$\int_S \bar{\mathbf{P}} \cdot \mathbf{n} dS = \bar{\mathbf{P}} \cdot \mathbf{n} dS = \frac{\omega}{2} \mathrm{Im}\left\{ \mathbf{U}^{T*} \left( \mathbf{K}_2^T + ik\mathbf{K}_3 \right) \mathbf{U} \right\} \tag{26}$$

Expressions (24) and (26) allow the direct computation of the energy velocity defined by Eq. (22).

## 3. RESULTS

Without loss of generality for the proposed method, the material is assumed to be isotropic with a Poisson coefficient of 0.30. The longitudinal and shear bulk velocities are defined as:

$$c_l = \sqrt{\frac{E(1-\nu)}{\rho(1+\nu)(1-2\nu)}} \quad , \quad c_s = \sqrt{\frac{E}{2\rho(1+\nu)}} \tag{27}$$

We consider waveguides with a circular cross-section of radius *a*, meshed with 3-node triangles. Variables are first adimensionalised with some characteristic length and time, chosen as *a* and $\omega/c_s$ respectively. Hence, the dimensionless frequency is given by

$\Omega = \omega a / c_s$. The step of a helix is given by $L = 2\pi R / \tan\phi$, where $\phi$ denotes the helix lay angle. The eigenproblem is solved using an algorithm based on the generalized Jacobi method, with bounds for the eigenvalue searching interval set to $|\mathrm{Im}(k)| \leq \gamma$ (where $\gamma$ is a user-defined parameter).

### 3.1. Convergence and accuracy

In order to assess the convergence and accuracy of the numerical method, FE results have been computed with a sequence of four refined meshes, shown in Fig. 1b with characteristics given in Table I. The successive refinements have been made by dividing each triangle of the previous cross-section mesh into four triangles. Plots of the dispersion error vs. the mesh fineness parameter 1/*h* are then obtained (*h* is chosen as the dimensionless maximum element length). The dispersion error is chosen as the ratio $\left|ka - k_{ref}a\right| / \left|k_{ref}a\right|$, where $ka$ and $k_{ref}a$ are respectively the adimensional FE and reference axial wavenumbers. Also shown in Table I is the rough criterion given by the ratio $\lambda_s/h$ (where $\lambda_s = 2\pi/\Omega$ is the dimensionless shear wavelength), often used in FEM methods to characterize the fineness of a mesh at a given frequency.

The numerical model is first validated with the Pochhammer-Chree semi-analytical model [1,32] describing elastic propagation in an infinite isotropic cylinder (i.e. $L \to \infty$). FE and analytical axial wavelengths are compared for a given dimensionless frequency $\Omega = 1$ and for solutions having the lowest imaginary parts: the $L(0,1)$ longitudinal mode

(propagating), the $F(1,1)$ flexural mode (propagating), the $F(1,2)$ flexural mode (evanescent), and the $F(2,1\ \&\ 2)$ mode (inhomogeneous), whose adimensional Pochhammer-Chree wavenumbers are respectively $k_{ref}a = 0.626$, $1.421$, $0.740i$, $0.953+1.905i$.

| No. | $h$ ($\lambda_s/h$) | # of elements | # of dofs |
|---|---|---|---|
| 1 | 1 (6) | 8 | 27 |
| 2 | 0.5 (12) | 32 | 75 |
| 3 | 0.25 (25) | 128 | 243 |
| 4 | 0.125 (50) | 512 | 867 |

TABLE 1: Characteristics of meshes (in parenthesis: $\lambda_s/h$ criterion for $\Omega$=1).

Figure 2a gives the convergence curve for each mode. It can be observed that the rate of convergence approaches a quadratic behaviour for every type of modes. The accuracy for the propagating bending mode is somewhat lower, as well as for the imaginary and complex solutions (corresponding to upper bending modes). As intuitively expected, a general trend for the accuracy of a given mode is to decrease as its order increases (i.e. as its modeshape becomes more and more complex). Note that the torsional mode ($k_{ref}a = 1$) is not shown because its SAFE wavenumber is almost

exact regardless of the mesh. The same results have already been reported by Damljanovic et al. [13].

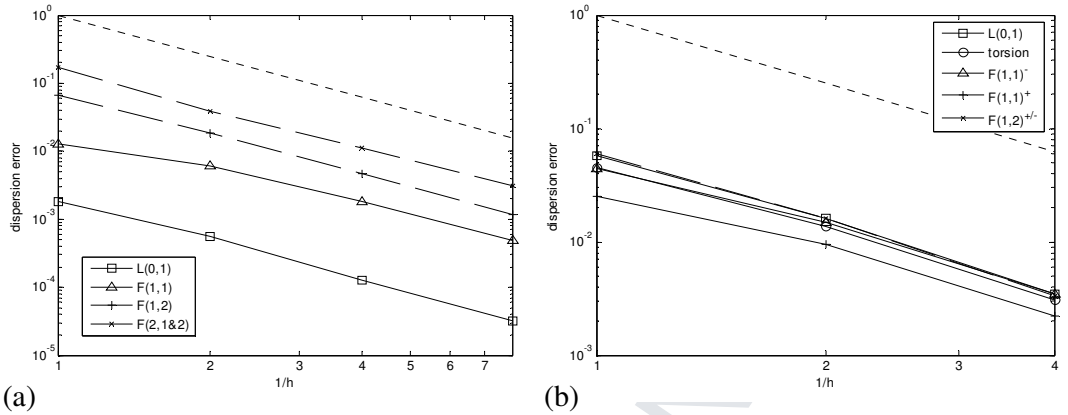


(a) (b)

FIG.2: (a) Dispersion error for the cylinder ($\phi$=0°) with respect to the Pochhammer-Chree solution (subscript $p$) vs. $1/h$ at $\Omega$=1 for the first propagating, evanescent and inhomogeneous modes. (b) Dispersion error for the helical waveguide ($\phi$=45°) with respect to the reference solution ($\lambda_s$/50 mesh) for the first modes. As a reference, the dotted line is the quadratic rate $(1/h)^2$.

The SAFE method is now tested for a helical waveguide having a strong lay angle $\phi$=45° and a helix radius $R$=2$a$. Table 2 gives a comparison of wavenumbers obtained for $\Omega = 1$ and mesh 4 with the FE periodic approach proposed by the author [25] (the notation −/+ is explained further below). A perfect agreement is obtained, the difference being less than 0.1% for each wavenumber. Figure 2b also gives the convergence curve for meshes 1 to 3 (because no analytical solution is available, the solutions obtained with the most refined mesh, mesh 4, is chosen as the reference). The rate of

convergence also approaches a quadratic behaviour. Note that the same trend is also obtained for the frequency error when solving the eigenproblem (19) with fixed real wavenumbers (results not shown for conciseness of the paper).

| | $L(0,1)$ | Torsion | $F(1,1)^{-}$ | $F(1,1)^{+}$ | $F(1,2)^{+/-}$ |
|---|---|---|---|---|---|
| SAFE | 0.6038 | 0.8775 | 1.2756 | 1.7162 | 0.2524+0.7153i |
| Periodic FE | 0.6041 | 0.8777 | 1.2752 | 1.7149 | 0.2525+0.7153i |

TABLE 2: First adimensional wavenumbers of the helical waveguide ($\phi$=45°) computed with the proposed SAFE method and the periodic FE method (Ref. [25]) for $\Omega$=1 with mesh 4 ($\lambda_s/h$=50 criterion).

From Fig. 2, a dispersion error less than 1% is reached for all modes with mesh 3. It can be concluded that a rough criterion of $\lambda_s/h$=25 is thus quite acceptable, which may be not the case for $\lambda_s/h$=10. Note that it coincides well with the criterion proposed for SAFE methods by Galan et al. [33,34] when using 3-node triangles.

### 3.2. Dispersion analysis of helical waveguides

#### 3.2.1. Analysis of a typical helical wire in civil engineering

The wave modes propagating inside a peripheral wire constituting a typical seven-wire strand is numerically studied. The helix radius of such a peripheral wire is $R$=2$a$

with a lay angle of 7.5° (for a typical radius $a$=2.5mm, it corresponds to a step $L$=23.9cm). In order to demonstrate the capability of the proposed method, some material damping is included in the analysis. A frequency independent hysteretic model is chosen with longitudinal and shear bulk wave attenuations respectively given by $\kappa_l$=0.003 and $\kappa_s$=0.043 Np/wavelength (typical properties for steel). The complex bulk velocities are then calculated as:

$$\tilde{c}_{l,s} = c_{l,s}\left(1 + i\frac{\kappa_{l,s}}{2\pi}\right)^{-1} \tag{28}$$

and the complex Young's modulus and Poisson's ratio can be obtained from:

$$\tilde{E} = \rho\tilde{c}_s^2\left(\frac{3\tilde{c}_l^2 - 4\tilde{c}_s^2}{\tilde{c}_l^2 - \tilde{c}_s^2}\right) \quad , \quad \tilde{\nu} = \frac{1}{2}\left(\frac{\tilde{c}_l^2 - 2\tilde{c}_s^2}{\tilde{c}_l^2 - \tilde{c}_s^2}\right) \tag{29}$$

Figure 3 shows the dispersion curves obtained for both the cylindrical and helical geometry. The eigensystem (21) has been solved by fixing the adimensional frequency Ω, ranging from 0 to 5 divided into five hundred steps. Following the conclusions drawn previously, a rough criterion of $\lambda_s/h$=20 at $\Omega = \Omega_{max} = 5$ has been chosen for the mesh (generating 2564 triangles and 3999 dofs). Because wavenumbers occur in pairs of opposite signs, only eigensolutions with positive real parts are plotted in Fig. 3. The absolute values of imaginary parts are also plotted on the same axis, which is more readable than a three-dimensional plot (note that the sign information is lost because imaginary parts are not necessarily positive). Every mode is attenuated in damped

media: in order to distinguish so-called quasi-propagating modes (in black on figures) from non-propagating modes (in grey), a limit $\mathrm{Im}(ka) \le 0.1$ has been set.

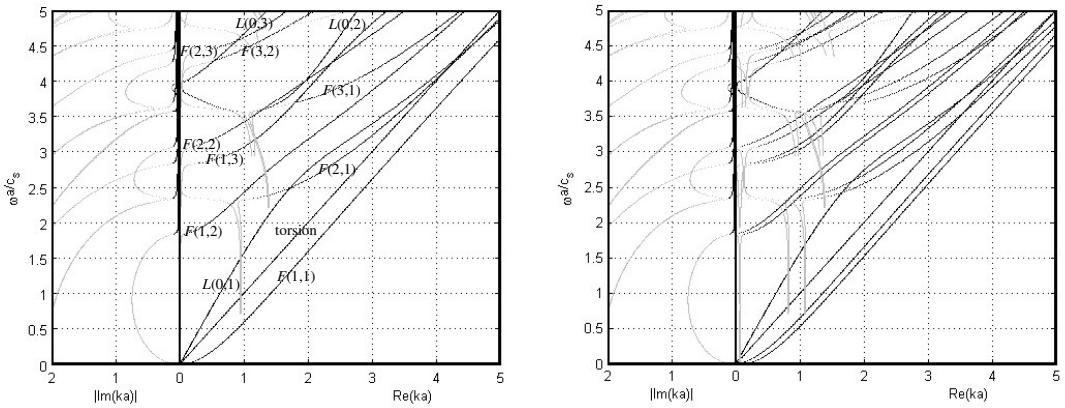


(a) (b)

FIG.3: Dispersion curves for Ω ranging from 0 to 5 (searching interval restricted to modes with |Im(*ka*)≤2|). Left: cylinder, right: helical $\phi$=7.5°. Black lines: quasi-propagating modes (|Im(*ka*)≤0.1|), grey lines: non-propagating modes (|Im(*ka*)>0.1|).

From a physical point of view, an interesting feature can be observed by comparing the cylindrical and helical cases. The wavenumbers of the compressional *L*(0,1) and the torsional modes are nearly unchanged by the helical geometry (provided that the helix arc length is considered). This is not the case for flexural modes, which occur in distinct roots instead of double roots because of the lack of symmetry of the helical geometry. A similar phenomenon was observed by Demma et al. [16] for toroidal waveguides when studying bends in pipelines. For simplicity, and though this notation may be somewhat

abusive, the pairs of helical flexural modes identified from their cylindrical counterparts have been denoted with superscripts + and – in this paper. It should also be outlined that the dispersion curves obtained in Fig. 3 are quite coherent with undamped results already obtained in Ref. [25].

Figure 4 plots the adimensional energy velocity and attenuation vs. adimensional frequency. It is clear that energy velocities and attenuations are almost unaffected by the helical geometry for $\phi$=7.5°. As can be observed for instance, compressional modes remain faster and less attenuated than flexural and torsional modes (which makes them suitable for non-destructive testing). The only slight difference that might be observed is the existence of some local variations (see inset in Fig. 4). A further investigation shows that these variations happen for branches that would disconnect in the undamped case (similar phenomena have already been reported in the literature – see [35] for instance).

In a very low frequency range, strong differences occur in the helical case so that a direct analogy with the cylinder becomes difficult. Dispersion curves have been plotted between $\Omega = 0$ and 0.02 in Fig. 5. The torsional and $L(0,1)$ modes are respectively cut-off near $\Omega$=0.010 and 0.014 (for the cylinder, these modes are always propagative). Under $\Omega$=0.009, it becomes difficult to distinguish which modeshape corresponds to a compressional or torsional behaviour: $l$ and $t$ notations have been replaced to denote respectively compression and torsion dominant modes (but the choice may be somewhat very subjective). Under 0.002, both modes propagate again and one of them has a

negative energy velocity. Finally, it should be outlined that Fig. 5a greatly coincides here again with the undamped results of Ref. [25] (though material damping is included in the present analysis).

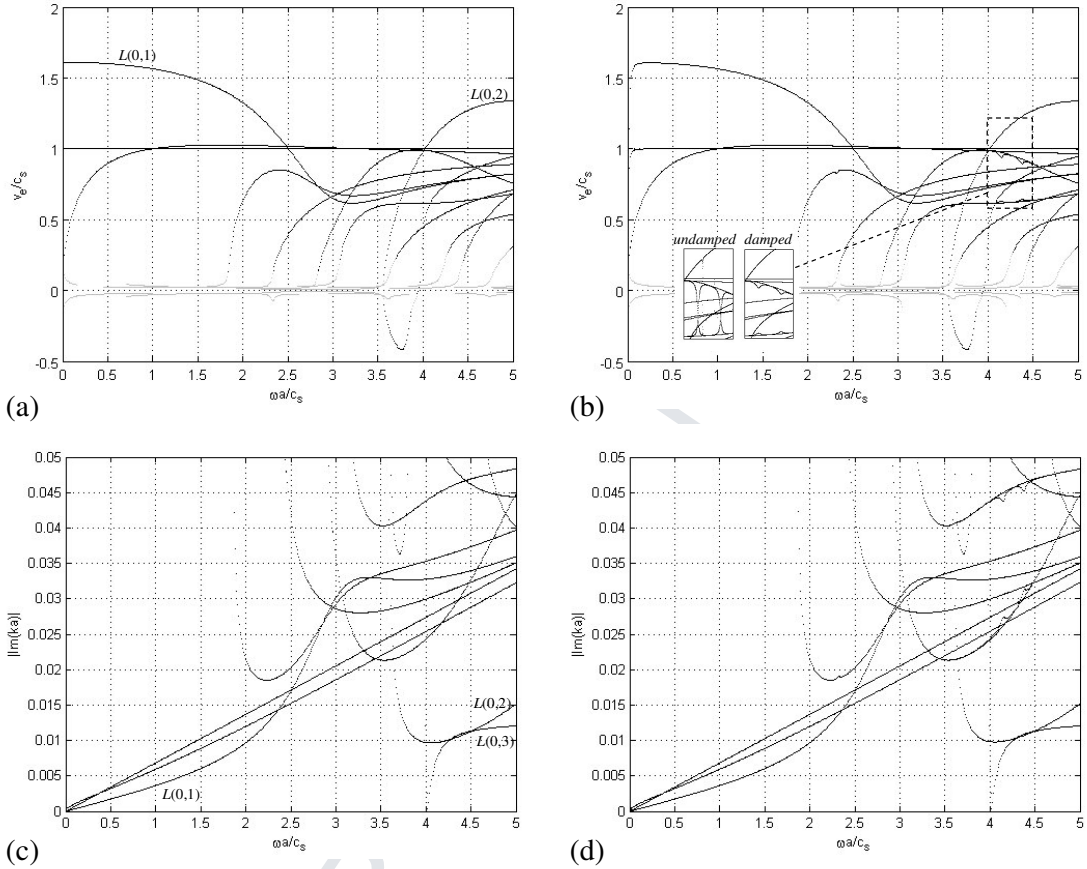


FIG.4: Adimensional energy velocity vs. frequency for (a) the cylinder and (b) the helical waveguide ($\phi$=7.5°). Attenuation |Im($ka$)| vs. frequency for (c) cylindrical and (d) helical waveguides. Inset: damped (current) and undamped results exhibiting some branch connections.

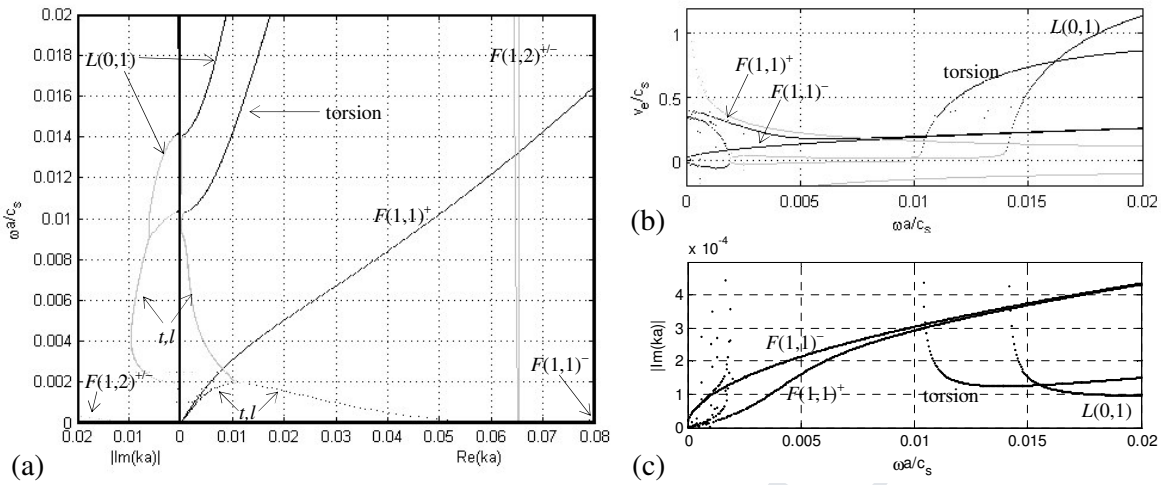


FIG.5: (a) Dispersion curves for Ω ranging from 0 to 0.02 (helical $\phi$=7.5°). Black lines: quasi-propagating modes (|Im($ka$)≤0.001|), grey lines: non-propagating modes (|Im($ka$)>0.001|). (b) Adimensional energy velocity and (c) attenuation vs. frequency.

### 3.2.2. Dispersion analysis for varying helix parameters

The effects of helix lay angle and radius are now briefly examined. Figure 6 exhibits the dispersion curves of propagating modes obtained for $R$=2$a$ and a lay angle varying from 0° (cylinder) to 75°. Note that the condition $L \geq 2a$, i.e. $\phi \leq \tan^{-1} \pi R/a$, is satisfied in order for cross-sections not to intersect each other between two successive turns. Material damping is neglected. Dispersion curves have been obtained with the same mesh as before. The eigenproblem (19) has been solved by computing the eigenfrequencies for fixed real wavenumbers $ka$ ranging from 0 to 5 divided into five hundred steps.

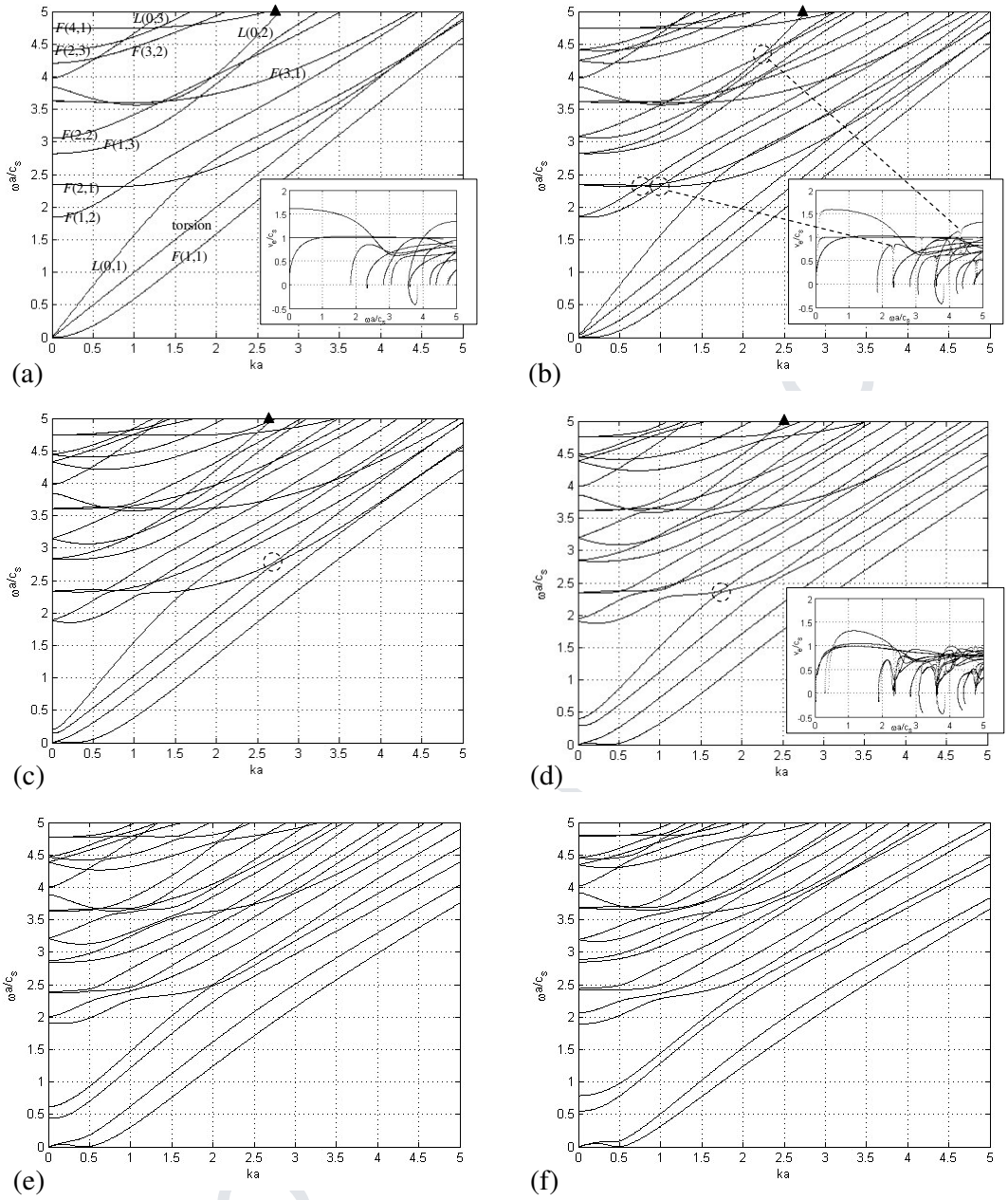


FIG.6: Dispersion curves of helical waveguides (without material damping) with $R$=2$a$ and a lay angle equal to: (a) 0° (cylinder), (b) 15°, (c) 30°, (d) 45°, (e) 60°, (f) 75°. Dashed circles: some examples of branch disconnections. Insets: plots of adimensional energy velocity vs. frequency. ▲: $L$(0,2) mode identified at Ω=5.

As previously, it can be clearly observed that every pair of flexural modes, which occurs in double roots in the cylinder case, becomes distinct in helical waveguides, while torsional and compressional modes are less affected. As expected, differences between cylinder and helical waveguides become greater as the lay angle increases (see Figs 6a-c). Their behaviour becomes quite different for $\phi \geq 45°$, even for torsion-like and compression-like modes (Figs. 6d-f). This is also illustrated for the energy velocities plotted for $\phi = 0°$ and 45° in the inset of Fig. 6a and 6d respectively. What is also observed is that the torsional and $L(0,1)$ modes are cut-off in a low frequency range, with increasing cut-off frequencies as the lay angle increases.

Furthermore, the number of branch disconnections tends to increase, as well as the distance between them. Some of these disconnections have been identified with dashed circles in Figs. 6b-d. As shown by comparing the insets of Figs. 6a-b, they are related with strong local variations of energy velocity. However, it should be reminded that some branch disconnections could actually be connected in the presence of damping (as previously observed for $\phi = 7.5°$). As an example, Fig. 7 illustrates the lay angle influence upon the $L(0,2)$ modeshape, identified at $\Omega = 5$ for $\phi = 0°$, 15, 30 and 45°.

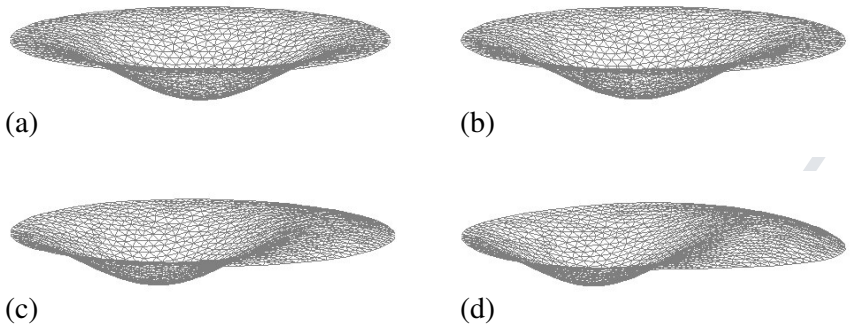


FIG.7: Real part of displacement for the $L(0,2)$ modeshape (deformed mesh) computed at $\Omega$=5 for (a) $\phi$=0°, (b) 15°, (c) 30°, (d) 45°.

It should be noted that results obtained with an increasing helix radius for a given lay angle exhibit a decreasing helix effect on wave propagation. As an example, if we increase the radius to $R$=10$a$ with $\phi$=90° – which corresponds to a toroidal waveguide – the behaviour of an infinite cylinder is surprisingly quasi-recovered as shown in Fig. 8.

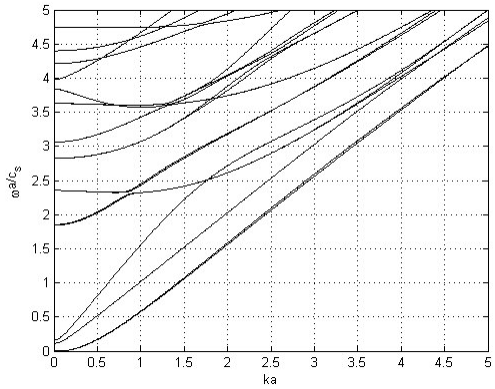


FIG.8: Dispersion curves of a toroidal waveguide ($\phi$=90°) with $R$=10$a$.

## 4. CONCLUSIONS

Elastic wave propagation inside helical waveguides has been analyzed through a SAFE method based on a non-orthogonal curvilinear coordinate system that is translationally invariant along the helix centreline. Some useful expressions of the cross-section and time averaged energy and flux have been proposed in order to directly compute the energy velocity. The convergence and accuracy of the proposed method have been studied and were shown to be similar to results found in the literature dealing with standard SAFE methods. With three-node triangles, a criterion of about $\lambda_s/20$ can be applied to generate the FE mesh.

From a physical point of view, the dispersion curves of a helical waveguide exhibit several differences compared with the cylinder. Provided that the arc length of the helix centreline is considered, the wavenumbers and energy velocities of compression modes are less affected than flexural modes. The latter do not occur in pairs of equal wavenumbers due to the lack of symmetry of the helical geometry. There exist some low-frequency bandcut zones where both the compressional and torsional modes become non-propagating. Some branch disconnections occur – generally yielding a significant decrease of the energy velocity – but some of these disconnections are likely to disappear when some material damping is taken into account. All the above-mentioned effects are stronger as the lay angle increases and as the helix radius decreases, until giving a quite different overall behaviour compared to the infinite cylinder.

**ACKNOWLEDGEMENT**

The author wishes to thank Dr. Laurent Laguerre, Laboratoire Central des Ponts et Chaussées, for helpful discussions and references.

## REFERENCES

[1] J. Zemanek, "An experimental and theoretical investigation of elastic wave propagation in a cylinder," Journal of the Acoustical Society of America **51**, 265–283 (1972).

[2] P. Rizzo, and F. Lanza di Scalea, "Load Measurement and health monitoring in cable stays via guided wave magnetostrictive ultrasonics," Materials Evaluation **62**, 1057–1065 (2004).

[3] H. Kwun, K. A. Bartels, and J. J. Hanley, "Effects of tensile loading on the properties of elastic-wave propagation in a strand," Journal of the Acoustical Society of America **103**, 3370–3375 (1998).

[4] M. D. Beard, M. J. S. Lowe, and P. Cawley, "Ultrasonic guided waves for inspection of grouted tendons and bolts," Journal of Materials in Civil Engineering **212**, 212–218 (2003).

[5] P. Rizzo, and F. Lanza di Scalea, "Wave propagation in multi-wire strands by wavelet-based laser ultrasound," Experimental Mechanics **44**, 407–415 (2004).

[6] P. Rizzo, "Ultrasonic wave propagation in progressively loaded multi-wire strands," Experimental Mechanics **46**, 297–306 (2006).

[7] L. Laguerre, J.-C. Aime, M. Brissaud, "Magnetostrictive pulse-echo device for non-destructive evaluation of cylindrical steel materials using longitudinal guided waves," Ultrasonics **39**, 503–514 (2002).

[8] B. N. Pavlakovic, M. J. S. Lowe, and P. Cawley, "High-frequency low-loss ultrasonic modes in imbedded bars," Journal of Applied Mechanics **68**, 67–75 (2001).

[9] L. Gavric, "Computation of propagative waves in free rail using a finite element technique," Journal of Sound and Vibration **185**, 531–543 (1995).

[10] N. Rattanawangcharoen, W. Zhuang, A. H. Shah, and S. K. Datta, "Axisymmetric guided waves in jointed laminated cylinders," Journal of Engineering Mechanics **123**, 1020–1026 (1997).

[11] W. Zhuang, A. H. Shah, and S. B. Dong, "Elastodynamic Green's function for laminated anisotropic circular cylinders," Journal of Applied Mechanics **66**, 665–674 (1999).

[12] T. Hayashi, W.-J. Song, and J. L. Rose, "Guided wave dispersion curves for a bar with an arbitrary cross-section, a rod and rail example," Ultrasonics **41**, 175–183 (2003).

[13] V. Damljanovic, and R. L. Weaver, "Propagating and evanescent elastic waves in cylindrical waveguides of arbitrary cross-section," Journal of the Acoustical Society of America **115**, 1572–1581 (2004).

[14] T. Hayashi, C. Tamayama, and M. Murase, "Wave structure of guided waves in a bar with an arbitrary cross-section," Ultrasonics **44**, 17–24 (2006).

[15] P. Wilcox, M. Evans, O. Diligent, M. Lowe, and P. Cawley, "Dispersion and excitability of guided acoustic waves in isotropic beams with arbitrary cross section," D. Thompson and D. Chimenti (eds), American Institute of Physics, Review of Progress in Quantitative NDE **21**, 203–210 (2002).

[16] A. Demma, P. Cawley, and M. Lowe, "The effect of bends on the propagation of guided waves in pipes," Journal of Pressure Vessel Technology **127**, 328–335 (2005).

[17] O. Onipede, S. B. Dong, and J. B. Kosmatka, "Natural vibrations and waves in pretwisted rods," Composite Engineering **4**, 487–502 (1994).

[18] O. Onipede, and S. B. Dong, "Propagating waves and end modes in pretwisted beams," Journal of Sound and Vibration **195**, 313–330 (1996).

[19] D. J. Mead, "Wave propagation in continuous periodic structures: research contributions from Southampton, 1964–1995," Journal of Sound and Vibration **190**, 495–524 (1996).

[20] D. J. Mead, "A general theory of harmonic wave propagation in linear periodic systems with multiple coupling," Journal of Sound and Vibration **27**, 235–260 (1973).

[21] A. Ghoshal, M. L. Accorsi, and M. S. Bennett, "Wave propagation in circular cylindrical shells with periodic axial curvature," Wave Motion **23**, 339–352 (1996).

[22] L. Gry, and C. Gontier, "Dynamic modeling of railway track: a periodic model based on a generalized beam formulation," Journal of Sound and Vibration **199**, 531–558 (1997).

[23] B. R. Mace, D. Duhamel, and M. J. Brennan, "Finite element prediction of wave motion in structural waveguides," Journal of the Acoustical Society of America **117**, 2835–2843 (2005).

[24] D. Duhamel, B. R. Mace, and M. J. Brennan, "Finite element analysis of the vibrations of waveguides and periodic structures," Journal of Sound and Vibration **294**, 205–220 (2006).

[25] F. Treyssede, "Numerical investigation of elastic modes of propagation in helical waveguides," Journal of the Acoustical Society of America **121**, 3398–3408 (2007).

[26] J. L. Synge, A. Schild, Tensor Calculus, Dover (1978).

[27] W.L. Neu, and H. Reismann, "Dynamics of the prestressed solids with application to thin shells," Solid Mechanics Archives **7**, 97–129 (1982).

[28] D. Chapelle, K. J. Bathe, The Finite Element Analysis of Shells – Fundamentals, Springer (2003).

[29] W. Sollfrey, "Wave propagation on helical wires," Journal of Applied Physics **22**, 905–910 (1951).

[30] A. Nicolet, F. Zola, and S. Guenneau, "Modeling of twisted optical waveguides with edge elements," The European Physical Journal Applied Physics **28**, 153–157 (2004).

[31] A. Bernard, M. J. S. Lowe, and M. Deschamps, "Guided waves energy velocity in absorbing and non-absorbing plates," Journal of the Acoustical Society of America **110**, 186–196 (2001).

[32] T. R. Meeker, and A. H. Meitzler, "Guided wave propagation in elongated cylinders and plates," *Physical Acoustics* (Academic, New York, 1964), Vol. 1, Sec. A2.

[33] J. M. Galan, and R. Abascal, "Elastodynamic guided wave scattering in infinite plates," International Journal for Numerical Methods in Engineering **58**, 1091–1118 (2003).

[34] J. M. Galan, and R. Abascal, "Lamb mode conversion at edges. A hybrid boundary-element–finite-element solution," Journal of the Acoustical Society of America **117**, 1777–1784 (2005).

[35] I. Bartoli, A. Marzani, F. Lanza di Scalea, and E. Viola, "Modeling wave propagation in damped waveguides of arbitrary cross-section," Journal of Sound and Vibration **295**, 685–707 (2006).